Bioactive Materials 20 (2023) 663–676

Contents lists available at ScienceDirect

Bioactive Materials

journal homepage: www.keaipublishing.com/en/journals/bioactive-materials

A novel cascaded energy conversion system inducing efficient and precise cancer therapy

Yong Kang [b,1], Na Kong [a,1], Meitong Ou [c], Ying Wang [c], Qicai Xiao [c], Lin Mei [c], Bing Liu [d], Liqun Chen [b,**], Xiaobin Zeng [a,***], Xiaoyuan Ji [b,*]

[a] Center Lab of Longhua Branch and Department of Infectious Disease, Shenzhen People's Hospital (The Second Clinical Medical College, Jinan University, The First Affiliated Hospital, Southern University of Science and Technology), Shenzhen, 518020, Guangdong, China
[b] Academy of Medical Engineering and Translational Medicine, Medical College, Tianjin University, Tianjin, 300072, China
[c] School of Pharmaceutical Sciences (Shenzhen), Sun Yat-sen University, Guangzhou, 510275, China
[d] Department of Disease Control and Prevention, Rocket Force Characteristic Medical Center, 16 Xinjiekouwai Street, Xicheng District, Beijing, 10088, China

ARTICLE INFO

Keywords:
Thermoelectric therapy
Photothermal therapy
Reactive oxygen species
p-n heterojunction
Energy conversion

ABSTRACT

Cancer therapies based on energy conversion, such as photothermal therapy (PTT, light-to-thermal energy conversion) and photodynamic therapy (PDT, light-to-chemical energy conversion) have attracted extensive attention in preclinical research. However, the PTT-related hyperthermia damage to surrounding tissues and shallow penetration of PDT-applied light prevent further advanced clinical practices. Here, we developed a thermoelectric therapy (TET) based on thermoelectric materials constructed p-n heterojunction ($SrTiO_3/Cu_2Se$ nanoplates) on the principle of light-thermal-electricity-chemical energy conversion. Upon irradiation and natural cooling-induced the temperature gradient (35–45 ^{o}C), a self-build-in electric field was constructed and thereby facilitated charges separation in bulk $SrTiO_3$ and Cu_2Se. Importantly, the contact between $SrTiO_3$ (n type) and Cu_2Se (p type) constructed another interfacial electric field, further guiding the separated charges to re-locate onto the surfaces of $SrTiO_3$ and Cu_2Se. The formation of two electric fields minimized probability of charges recombination. Of note, high-performance superoxide radicals and hydroxyl radicals' generation from O_2 and H_2O under catalyzation by separated electrons and holes, led to intracellular ROS burst and cancer cells apoptosis without apparent damage to surrounding tissues. Construction of bulk and interfacial electric fields in heterojunction for improving charges separation and transfer is also expected to provide a robust strategy for diverse applications.

1. Introduction

Very recently, with the rapid development of nanotechnology and nanomedicine, energy-conversion material-mediated therapies have aroused comprehensive attention due to their non-invasive feature and reliable therapeutic effect. Among them, photothermal therapy (PTT) based on light-thermal conversion and photodynamic therapy (PDT) based on light-chemical energy conversion are the most representative energy-conversion therapies [1–5]. To achieve a high anticancer efficiency, two essential criteria of traditional PTT and PDT should be considered, including high light-thermal or light-chemical energy conversion performance of the employed agents and long light penetration with minimized tissue scattering and absorption [6–9]. Typically, energy conversion efficiency is the critical factor for an eligible nanomedicine. For example, it is quite necessary for a photothermal agent to increase the temperature of the tumor site above 50 °C for achieving a desired therapeutic outcome. Additionally, in order to improve light penetration, great endeavors have been devoted to develop the second near infrared ray-based materials (NIR-II) in the spectra range of 1000–1350 nm, which possesses deeper tissue-penetration, reduced

Peer review under responsibility of KeAi Communications Co., Ltd.
* Corresponding author.
** Corresponding author.
*** Corresponding author.
E-mail addresses: liqun.chen@tju.edu.cn (L. Chen), zeng.xiaobin@szhospital.com (X. Zeng), jixiaoyuan@tju.edu.cn (X. Ji).
[1] Y. K. and N. K. contributed equally to this work.

https://doi.org/10.1016/j.bioactmat.2022.07.007
Received 30 December 2021; Received in revised form 18 June 2022; Accepted 5 July 2022

light scattering, and higher skin permissible exposure (MPE) than that of NIR-I and visible light [10–14]. Nevertheless, only limited examples of NIR-II photothermal agents and negligible NIR-II photodynamic agents have been reported. Besides, the tissue-penetration of NIR-II light was greatly affected by the strong absorbance band of water overtone, causing potential thermal damage to normal organs and tissues [15–18]. Therefore, despite these great advances achieved to date, most of the existing PDTs are limited to superficial treatments, and most of the existing PTTs are not specifically related to cancer-associated events. That is, although light irradiation could target the tumor site, hyperthermia induced by conventional photothermal agents or ambient fluid body, would randomly propagate and diffuse to the surrounding normal tissues and organs, and thus results in the treatment-related toxicity and side effects, which are the major obstacle preventing further advanced clinical practice of PTT.

Over the last few decades, thermoelectric (TE) materials, through converting thermal to electricity *via* electron-hole pairs separation under temperature gradient-induced the build-in thermoelectric field, have attracted tremendous attention worldwide in materials science and solid-state physics, due to their wide application in Peltier cooling and waste energy harvesting [19–25]. Further analysis of the mechanism of TE materials shows the separated electron-hole pairs under build-in thermoelectric field demonstrating great potentials in catalyzing reactive oxygen species (ROS) generation in cushy conditions, similar with the mechanisms of photodynamic therapy and piezocatalytic therapy [26,27]. In addition, compared with PTT-generated hyperthermia, the ROSs have much shorter lifetime and propagation distance *in vivo*, presumably guaranteeing much less treatment-related side effect or toxicity on surrounding normal tissues and organs. Although TE generators have grown into superstars in the application fields of energy and environment, it is still an infant in biomedical fields. Typically, the thermoelectric figure of merit is the key to evaluate the efficiency of TE materials, $ZT = S^2\sigma T/\kappa$, where S, σ, T and κ represents Seebeck coefficient, electrical conductivity, temperature, and thermal conductivity, respectively [28,29]. Obviously, the thermoelectric efficiency not only relates to physicochemical properties of TE materials, such as Seebeck coefficient, electrical conductivity, and thermal conductivity, but it also has a linear correlation with the operating temperature, in which higher temperature endows more effective electron-hole pairs separation and higher thermoelectric efficiency, which is also the main obstacle for applications in biomedical fields of TE materials [30]. Based on our previous studies [31–36], heterojunction construction, including p-n junction and Z scheme junction, has been demonstrated as an efficient strategy for improving electron-hole pairs separation and enhancing the catalytic efficiency. After contacting of p-type and n-type semiconductors, the interfacial electric field will be constructed, in which the separated electrons and holes in both semiconductors would transfer in the opposite direction and locate in different semiconductors [37–40]. The unfavorable recombination of electron-hole pairs would be retarded, which is the key for conversion efficiency of photocatalysts,

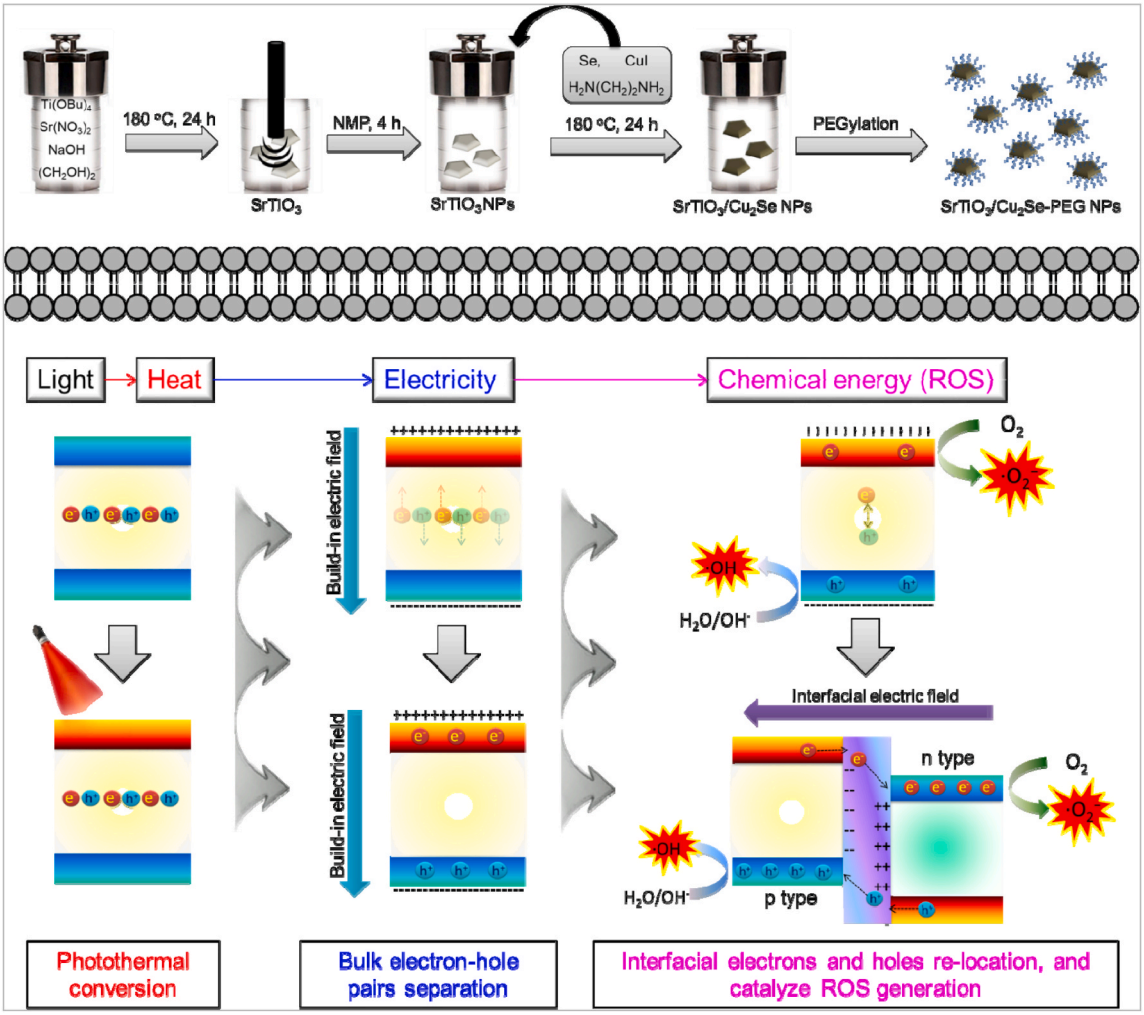

Scheme 1. Schematic illustration of preparation and mechanism of $SrTiO_3/Cu_2Se$ p-n heterojunction based thermoelectric therapy (TET). $SrTiO_3/Cu_2Se$ p-n heterojunction was fabricated through two steps hydrothermal process.

electrocatalysts, and TE materials.

Herein, for the first time, we developed a novel thermoelectric therapy (TET) based on light-thermal-electricity-chemical energy conversion, by employing $SrTiO_3$ (n type) and Cu_2Se (p type) to construct a p-n heterojunction, which is capable of dual independently targeted generating ROS under mild temperature gradient (from 35 °C to 45 °C). As shown in Scheme 1, by employing conventional two-step hydrothermal processes, $SrTiO_3/Cu_2Se$ based p-n heterojunction was constructed. Under 808 nm laser irradiation and natural cooling, the electrons and holes in the bulk of $SrTiO_3$ and Cu_2Se voluntarily separate and migrate from the bulk to the surface under the driving force of the build-in thermoelectric field on the opposite directions. Additionally, the p-n heterojunction between $SrTiO_3$ and Cu_2Se constructs an interfacial electric field, and thus redistributes the surface electrons and holes to specific locations for reduction and oxidation reactions, respectively, which further restrains the undesired recombination of electrons-hole pairs in the bulk and on the surface of TE materials. Consequently, a ROS burst under mild temperature gradient and low concentration of TE materials was provided based on a thermoelectric effect. With the goal of complete remission of tumors and without recurrence, our work here presents a novel thermoelectric mechanism based on p-n heterojunction constructed TE generator, with dual independently targeted ROS bursts for efficient cancer therapy and with negligible side effects towards normal tissues. To be noted, we also anticipate the performances of such a p-n heterojunction-constructed TE generator in other settings of biomedical applications beyond cancer treatment.

2. Materials and methods

2.1. Materials

$Ti(OBu)_4$, $Sr(NO_3)_2$, NaOH, $(CH_2OH)_2$, Se, CuI, $H_2N(CH_2)NH_2$, 9,10-anthracenedipropanoic acid (ABDA), $[Ru(dpp)_3]Cl_2$ (RDPP), H_2O_2 (30%), N-methyl-pyrrolidone (NMP), methylene blue (MB), 5,5′-dithiobis (2-nitrobenzoic acid) (DTNB), and dihydrorhodamine 123 (DHR123) were supplied by Sigma-Aldrich.DSPE-PEG-Cy7 (MW: 5k) and DSPE-PEG (MW: 5k) were purchased from Nanocs Inc. PBS (pH 7.4 and 5.5), DMEM medium, RPMI medium, trypsin-EDTA, and fetal bovine serum (FBS) were purchased from Gibco Life Technologies.

2.2. Synthesis of $SrTiO_3/Cu_2Se$ NPs

The $SrTiO_3/Cu_2Se$ NPs based p-n heterojunction was prepared by simple two-step hydrothermal processes. First, $SrTiO_3$ NPs were synthesized by a hydrothermal method using Teflon lined stainless steel autoclave containing the mixture of $(CH_2OH)_2$, NaOH, $Sr(NO_3)_2$, and $Ti(OBu)_4$. After the steel autoclave was heated at 180 °C for 24 h, the obtained powder was under probe sonication–assisted liquid exfoliation in NMP for 5 h. Then, the solution was centrifuged at 3000 rpm for 5 min to obtain $SrTiO_3$ NPs. For Cu_2Se QDs coating, CuI and Se powders were placed in a Teflon lined stainless steel autoclave containing 30 mL ethylenediamine and prepared $SrTiO_3$ NPs. After the steel autoclave was heated at 90 °C for 4 h, the precipitate was centrifuged at 3000 rpm and washed with distilled water for 3 times. Then, the prepared products were dried in vacuum at 50 °C for 4 h. The final black products ($SrTiO_3/Cu_2Se$ NPs) were collected.

For surface modification, 1,2-distearoyl-sn-glycero-3-phosphoethanolamine-N-polyethyleneglycol (DSPE-PEG) was dissolved into the $SrTiO_3/Cu_2Se$ NPs solution and stirred for 12 h after 30 min of sonication. Then the solution was centrifuged for 30 min at 5000 rpm with Amicon pipes (MWCO 100 kDa; Millipore) and the precipitates were washed 3 times to remove the residual DSPE-PEG. The same process was used for fluorescent modification of $SrTiO_3/Cu_2Se$ NPs using DSPE-PEG-Cy7 in a dark environment.

2.3. Characterization

The zeta potential and corresponding size of $SrTiO_3/Cu_2Se$ NPs were detected through Dynamic Light Scattering. The morphology of $SrTiO_3/Cu_2Se$ NPs was observed with transmission electron microscopy (TEM, JEM-2100UHR, JEOL, Japan) and atomic force microscopy (AFM, FASTSCANBIO, Germany). Piezoresponse force microscopic (PFM) measurements were characterized by an AFM (NTEGRA, NT-MDT, Russian) equipped with a ferroelectric test system. The $SrTiO_3/Cu_2Se$ NPs chemical constituents were detected by energy-dispersive X-ray spectroscope (EDS) (Inca X-MAX, Oxford, UK), X-ray photoelectron spectroscopy (XPS, ESCALAB 250Xi, Japan), and fourier transform infrared spectrophotometry (FTIR, Nexus 470, Nicolet, Madison, WI, USA). The $SrTiO_3/Cu_2Se$ NPs chemical structures were characterized by employing X-ray powder diffraction (XRD, Bruker D8 multipurpose). As for thermoelectric properties, a laser flash method (LFA 457, NETZSCH) was utilized to measure thermal diffusivity (D), while a ZEM-3, ULVAC was used for the analysis of σ and S.

2.4. ·OH production in vitro

The mixture of $SrTiO_3$ NPs, Cu_2Se QDs or $SrTiO_3/Cu_2Se$ NPs and MB were prepared in PBS (pH 7.4) and stirred for 1 h in a dark environment at the corresponding final concentration of 0.050 mg/mL TE agents and 0.05 mg/mL MB, respectively. Then the mixture was irradiated with 808 nm laser (1 W/cm^2) for 2.5 min and cooled naturally for 10 min. The diminished MB was determined by recording the absorption of the supernatant *via* UV–vis spectroscopy.

2.5. $\cdot O_2^-$ production in vitro

The mixture of $SrTiO_3$ NPs, Cu_2Se QDs or $SrTiO_3/Cu_2Se$ NPs (0.05 mg/mL) and DHR123 (1 μL,1 mM) were formed in PBS (pH 7.4) and stirred for 1 h in a dark environment. Then the mixed solution was irradiated *via* 808 nm laser (1 W/cm^2) for 2.5 min and natural cooling for 10 min. The changing fluorescence of DHR123 was recorded by fluorescence spectrophotometer.

2.6. Electron Paramagnetic Resonance (EPR) for ·OH and $\cdot O_2^-$ in vitro

For further detection of the ·OH and $\cdot O_2^-$ formation, $SrTiO_3/Cu_2Se$ NPs (0.05 mg/mL) and 5,5-dimethyl-1-pyrroline N-oxide (DMPO) (0.1 mM) were fully mixed (solution for testing ·OH: DI water, solution for testing $\cdot O_2^-$: methanol). The respective signals were analyzed by Electron Paramagnetic Resonance (EPR).

2.7. Cytotoxicity of TE agents

MCF 7 and Hela cells were plated and cultured in 96-well microplates (37 °C, 5% CO_2) for 24 h. Then the $SrTiO_3$ NPs, Cu_2Se QDs or $SrTiO_3/Cu_2Se$ NPs at different concentrations (ranging from 0.025 mg/mL to 0.1 mg/mL) were mixed into the culture medium. Following 24h co-incubation, MTT assay (Life Technologies) was conducted to determine cell viabilities according to the manufacturer's instructions.

2.8. Production of ROS in cells

After 24 h of culture (37 °C, 5% CO_2) in dishes, MCF 7 cells were incubated with the $SrTiO_3$ NPs, Cu_2Se QDs and $SrTiO_3/Cu_2Se$ NPs (final concentration of 0.05 mg/mL) respectively for another 24 h. Next, the DCFH-DA solution (final concentration of 0.2 μM) was put into the above medium and incubated for 0.5 h. Following removing the culture medium and washing with PBS, the cells were illuminated for 2.5 min employing an 808 nm light with power 1 W/cm^2 and cooled naturally for 10 min. The green fluorescence induced by ROS was detected by CLSM.

2.9. In vitro TET

MCF 7 and Hela cell lines were plated in 96-well plates and cultured for 24 h (37 °C, 5% CO_2). Then the $SrTiO_3$ NPs, Cu_2Se QDs or $SrTiO_3/Cu_2Se$ NPs at different concentrations (ranging from 0.025 mg/mL to 0.1 mg/mL) were mixed into the culture medium and incubated for another 24 h. Following culture medium removing and PBS washing, the cells were illuminated for 2.5 min employing an 808 nm light with power 1 W/cm^2 and cooled naturally for 10 min. After 24-h culture, the cells were washed with PBS for several times. MTT assay was applied to detect cell viability.

2.10. Pharmacokinetic study

To conduct *in vivo* pharmacokinetic study, 200 μL of Cy7 functionalized $SrTiO_3/Cu_2Se$ NPs (6 mg/kg) were i.v. injected in C57BL/6 mice. After different intervals, a microplate reader was utilized to test fluorescent intensity of Cy7 through the collected 20 μL blood.

2.11. In vivo imaging and biodistribution study

For the sale of fluorescence imaging and biodistribution study *in vivo*, 200 μL of Cy7 functionalized $SrTiO_3/Cu_2Se$ NPs (6 mg/kg) were i.v. injected into mice bearing MCF 7 tumors. The Maestro2 In-Vivo Imaging System was employed to detect the fluorescent intensity of tumor and major organs 24 h post-injection.

2.12. In vivo TET

After the tumors had reached to ~100 mm^3, mice were randomly allocated into 6 groups, 5 mice in each group. 1) saline control, 2) $SrTiO_3/Cu_2Se$ NPs, 3) $SrTiO_3$ NPs + ΔT, 4) Cu_2Se QDs + ΔT, 5) $SrTiO_3/Cu_2Se$ NPs + ΔT, 6) G + ΔT, and 7) PTT (G, >55 °C). The injected doses of $SrTiO_3/Cu_2Se$ NPs, $SrTiO_3$ NPs, and Cu_2Se QDs were 6 mg/kg. The ΔT means temperature gradient (35–45 °C) for 3 cycles inducing by 808 nm laser irradiation and natural cooling after 24 h post injection. The volume of tumors was monitored every two days lasting 14 days. All animal experiments were performed according to protocols approved by the Institutional Animal Care and Use Committee of Sun Yat-sen University (Guangzhou, China).

2.13. In vivo toxicity

C57BL/6 mice were i.v. injected with $SrTiO_3/Cu_2Se$ NPs (10 mg/kg) in order for toxicity analysis *in vivo*. Major organs were collected and subjected to eosin (H&E) and hematoxylin staining 30 days post-injection. Then the immune response was analyzed through the i.v. injection of $SrTiO_3/Cu_2Se$ NPs (10 mg/kg) into C57BL/6 mice. At 12 h and 24 h post-injection, ELISA was used to measure the concentrations of interleukin6 (IL-6), tumor necrosis factor-α (TNF-α) and interferon-γ (IFN-γ). At day1, 7, and 14 after intravenous injection, urea nitrogen (BUN), creatinine (Cr), albumin (ALB), total protein (TP), aspartate alanine aminotransferase (ALT), and aminotransferase (AST) were detected in a whole blood panel.

2.14. Statistical analysis

Data statistics and statistical significance were calculated by using Graph Pad Prism 8.0 and Origin 9.0. And NPs biodistribution and tumor volume were analyzed *via* employing Microsoft Excel 2016.

3. Results and discussion

3.1. Preparation and characterization of $SrTiO_3/Cu_2Se$ p-n heterojunction

In the first stage of this work, the $SrTiO_3/Cu_2Se$ p-n heterojunction was synthesized through two steps of hydrothermal process. Detailly, as illustrated in Scheme 1, $SrTiO_3$ nanoplates (NPs) (n type TE materials) were papered firstly following Cu_2Se quantum dots (QDs) synthesis and in site coating on the surface of $SrTiO_3$ NPs. After the hydrothermal process and liquid exfoliation, $SrTiO_3$ NPs with a size of 110 nm and a polydispersity index (PDI) of 0.182 were analyzed by transmission electron microscopy (TEM) (Fig. 1a and Fig. S1). Then, Cu_2Se QDs, p type TE materials, were synthesized and coated on the surface of $SrTiO_3$ NPs, forming a novel p-n heterojunction-based TE generator. The successfully coated Cu_2Se QDs was obviously observed in the TEM images of $SrTiO_3/Cu_2Se$ NPs (Fig. 1b), in which uniform QDs decoration on the surface of $SrTiO_3$ NPs was exhibited. The size and PDI of the prepared $SrTiO_3/Cu_2Se$ NPs were appropriately increased to about 132 nm and 0.256 (Fig. S2). Additionally, the high-resolution transmission electron microscopy (HRTEM) images with clear interference fringe and *d*-spacing of 0.27 nm and 0.33 nm, corresponding to the plane of $SrTiO_3$ NPs (Fig. 1c) and Cu_2Se QDs (Fig. 1d), provided direct evidence for the successful fabrication of the heterojunction structure. Besides, atomic force microscope (AFM) was also applied to characterize the morphology of the fabricated $SrTiO_3/Cu_2Se$ NPs. As shown in Fig. 1d and e, a rough surface was clearly observed, which was likely attributed to the coating of Cu_2Se QDs. Calculation from the 2D and 3D AFM images of $SrTiO_3/Cu_2Se$ NPs, the NPs displayed a planar size of about 132 nm and thickness of 50 nm. Given that almost all thermoelectric materials have a good piezoelectric property [41–43], we determined the piezoelectric properties of $SrTiO_3/Cu_2Se$ NPs by a piezoresponse force microscope (PFM), using dual alternating current resonance tracking (DART) modes with the aim to expel the displacement contribution from electrostatic interaction and topographical crosstalk in mapping the local electromechanical properties. Fig. 1e–h exhibited the topographic, vertical piezoresponse amplitude, and phase images of the $SrTiO_3/Cu_2Se$ NPs, respectively. The $SrTiO_3/Cu_2Se$ NPs can be clearly detected in the topographic image with clear contrast in the amplitude and phase images. Fig. 1g exhibited the phase map of $SrTiO_3/Cu_2Se$ NPs, which well matches the morphology map in Fig. 1e. Next, a surface potential of 30 mV of $SrTiO_3/Cu_2Se$ NPs was observed in the piezoelectric potential map of $SrTiO_3/Cu_2Se$ NPs (Fig. 1h) obtained by PFM in the darkness, which demonstrates its piezoelectric property and further testifies its thermoelectric property. To further confirm the successful fabrication and the composition of $SrTiO_3$ NPs, Cu_2Se QDs and $SrTiO_3/Cu_2Se$ NPs, X-ray photoelectron spectroscopy (XPS) and X-ray diffractometry (XRD) were performed. In the XPS analysis (Fig. 2a), the specific peaks of Sr, Ti, O, and Cu, Se, were exhibited in their XPS spectra, respectively. Moreover, all these characteristic peaks were observed in the XPS spectrum of $SrTiO_3/Cu_2Se$ NPs. For the XRD detection, as shown in Fig. 2b, the obtained $SrTiO_3$ NPs, Cu_2Se QDs, and $SrTiO_3/Cu_2Se$ NPs exhibited high phase purity, which is evidenced from their XRD pattern. The XRD peaks of $SrTiO_3$ NPs were well-matched with JCPDS card no. 35–0734 corresponding to cubic structured $SrTiO_3$ nanocrystals. The XRD peaks of Cu_2Se QDs were well-matched with and JCPDS card no. 29–0575 corresponding to tetragonal structured Cu_2Se nanocrystals. Moreover, the corresponding XRD peaks of $SrTiO_3$ NPs and Cu_2Se QDs were all observed in the XRD spectrum of $SrTiO_3/Cu_2Se$ NPs, which further demonstrated the successful synthesis of high purity $SrTiO_3/Cu_2Se$ NPs. All above observations confirmed the successful fabrication of the heterojunction structure and their potential thermoelectric property of $SrTiO_3/Cu_2Se$ NPs.

The biomedical applications of nanomedicine largely depend on their physiological dispersibility and stability. It was observed that the surfaces of $SrTiO_3/Cu_2Se$ NPs were slightly negatively charged after the

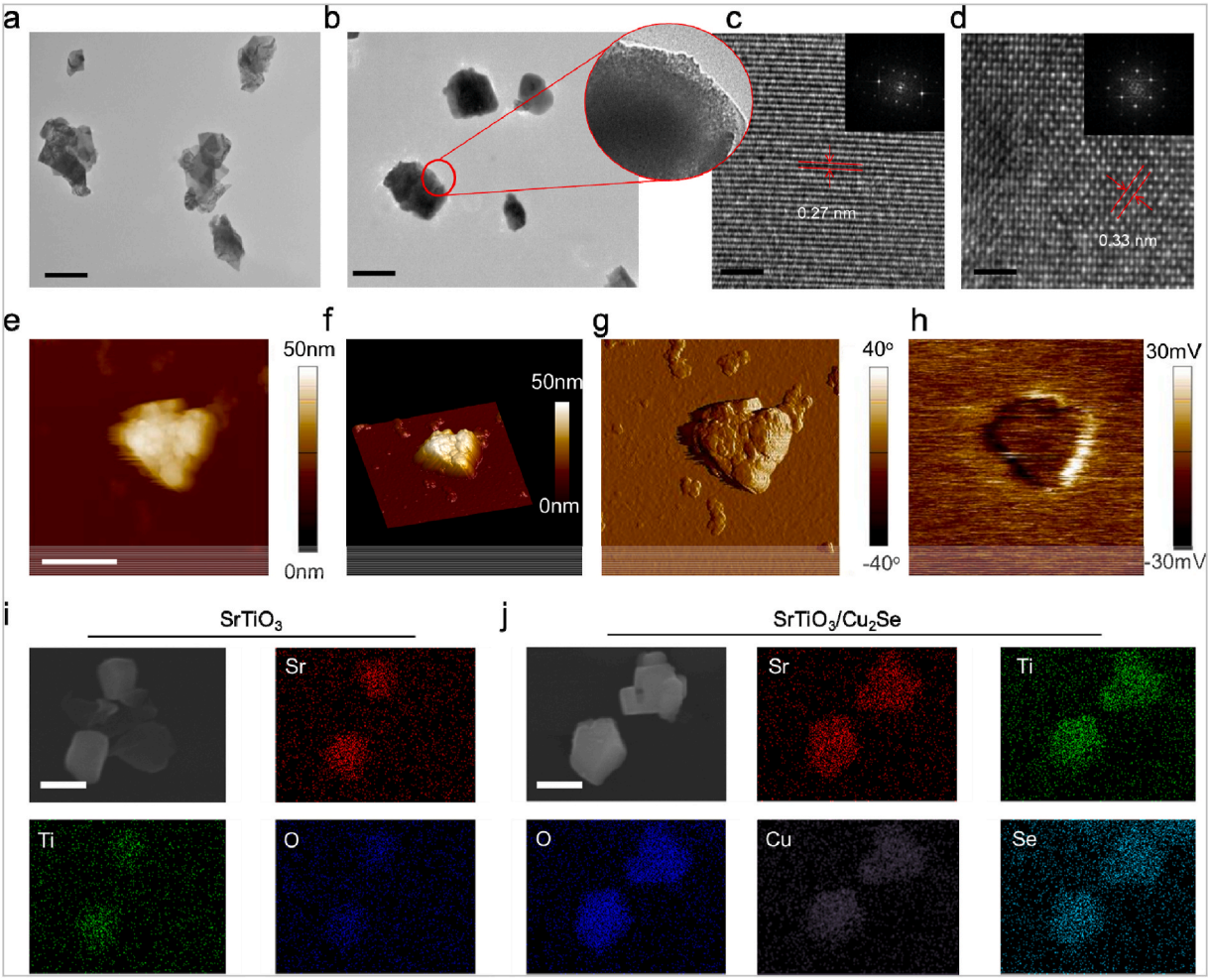

Fig. 1. Characterization of $SrTiO_3/Cu_2Se$ p-n heterojunction. (a) TEM images of $SrTiO_3$ NSs (scale bar 100 nm). (b) TEM images of $SrTiO_3/Cu_2Se$ NSs (scale bar 100 nm). (c) HRTEM image (inset: FFT diffraction patterns) of $SrTiO_3$ (scale bar 5 nm). (d) HRTEM image (inset: FFT diffraction patterns) of Cu_2Se (scale bar 5 nm). (e) 2D AFM image of $SrTiO_3/Cu_2Se$ NSs (scale bar 100 nm for all panels). (f) 3D AFM image of $SrTiO_3/Cu_2Se$ NSs. (g) phase image of the piezoelectric response of $SrTiO_3/Cu_2Se$ NSs. (h) piezoelectric potential of $SrTiO_3/Cu_2Se$ NSs. (i and j) SEM-EDX mapping images of $SrTiO_3$ and $SrTiO_3/Cu_2Se$ NSs (scale bar 100 nm for all panels).

hydrothermal process, (Fig. S3), which allowed surface modification by using amphipathic DSPE-PEG through hydrophobic interaction. The zeta potential of $SrTiO_3/Cu_2Se$ NPs increased to −30 mV, demonstrating a successful PEG modification and thus ensuring their physiological dispensability and stability. Around 25% (w/w) of DSPE-PEG was loaded on the surface of the $SrTiO_3/Cu_2Se$ NPs as measured by inductively coupled plasma-atomic emission spectrometry (ICP-AES). PEGylation of $SrTiO_3/Cu_2Se$ NPs showed improved dispersion in cell culture medium, phosphate buffer saline (PBS) and water in contrast with the bare $SrTiO_3/Cu_2Se$ NPs due to lack of aggregation (Fig. S4). And the size of $SrTiO_3/Cu_2Se$ NPs after PEGylation increased to 153 nm and the PDI of $SrTiO_3/Cu_2Se$ NPs after PEGylation decreased to 0.102. In addition, the Fourier transform infrared (FT-IR) absorption bands of the PEGylated $SrTiO_3/Cu_2Se$ NPs at ~1250 cm^{-1} and ~2900 cm^{-1} are corresponded to the C═O stretching vibration and –CH vibrations in the DSPE-PEG segment (Fig. S5). Finally, Sr (red), Ti (green), and O (blue) appeared in the energy dispersive spectrometry (EDS) mapping of $SrTiO_3$ NPs, and after Cu_2Se QDs and PEG coating, Cu (purple), Se (olive), C (yellow), and N (white) showed again in the EDS mapping of PEGylated $SrTiO_3/Cu_2Se$ NPs (Fig. 1i and Fig. S6), further confirmed successful surface coating by DSPE-PEG.

Next, the thermoelectric performance of our prepared $SrTiO_3/Cu_2Se$ NPs were examined. The ZT of $SrTiO_3$ NPs and Cu_2Se QDs were tested and calculated, respectively. Fig. 2c shows the material-dependent σ as a function of temperature. It is apparently that σ increases monotonically with increasing the temperature for these two samples and roughly follows a co-efficient of $T^{-1.5}$, suggesting that acoustic phonons dominate the carrier scattering. Fig. 2d shows the variations of S with the temperature. The positive signal of S indicates the p-type nature for Cu_2Se QDs, and the negative signal of S indicates the n-type nature for $SrTiO_3$ NPs. S increases gently upon increasing the temperature. Fig. 2e presents the plots of $S^2\sigma$ as a function of temperature, from which relatively high $S^2\sigma$ of $SrTiO_3$ NPs and Cu_2Se QDs were obtained. Fig. 2f is the plots of κ as a function of temperature, in which the relatively low κ of $SrTiO_3$ NPs and Cu_2Se QDs were also obtained. Due to the obtained high $S^2\sigma$ as well as low κ, significantly enhanced ZT values are expected. Fig. 2g is the ZT plots as a function of temperature, in which a peak ZT of 0.11 and 0.17 at 333 K is achieved in the fabricated $SrTiO_3$ NPs and Cu_2Se QDs. Fig. 2h shows the S at room temperature as a function of the natural logarithm of σ of $SrTiO_3$ NPs and Cu_2Se QDs. This linear relationship between the S and the natural logarithm σ indicates more fluctuating carrier concentration and less varying carrier mobility. All above observations confirmed the good thermoelectric properties of $SrTiO_3/Cu_2Se$ NPs.

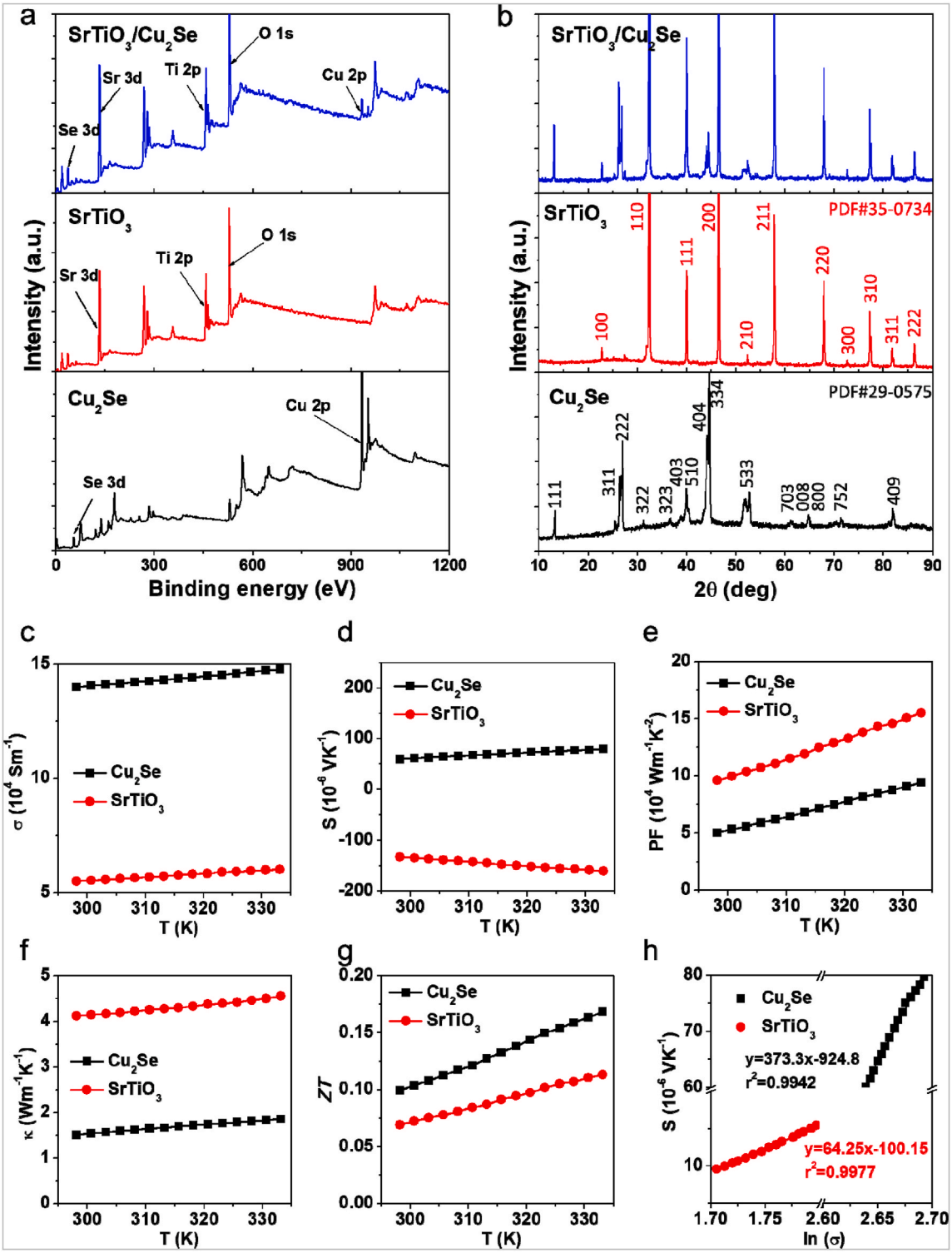

Fig. 2. Chemical composition and thermoelectric characterization. (a) XPS spectra of $SrTiO_3$ NSs, Cu_2Se NPs, and $SrTiO_3/Cu_2Se$ NSs. (b) XRD spectra of $SrTiO_3$ NSs, Cu_2Se NPs, and $SrTiO_3/Cu_2Se$ NSs. Thermoelectric characteristics of $SrTiO_3$ NSs and Cu_2Se NPs: (c) σ, (d) S, (e) PF (f) κ, (g) ZT, and (h) S vs ln (σ), respectively.

3.2. $SrTiO_3/Cu_2Se$ NPs mediated reactive oxygen species (ROS) generation

Followingly, the light-thermal-electricity-chemical energy conversion of $SrTiO_3$ NPs, Cu_2Se QDs, and $SrTiO_3/Cu_2Se$ NPs were measured and analyzed. In order to better prediction of application effects *in vivo*, the initial temperature was set at 35 °C. Fig. 3a and b shows the light-thermal conversion of $SrTiO_3/Cu_2Se$ NPs, in which the temperature increased from 35 °C to 45 °C under 2.5 min 808 nm laser irradiation and cooled down to 35 °C following 9 min natural cooling process. As shown in Fig. 3h, according to thermoelectric effect, under temperature gradient (35 °C–45 °C) induced by 808 nm laser irradiation and natural cooling, a build-in electric field was constructed on the opposite surfaces of $SrTiO_3$ NPs or Cu_2Se QDs. Therefore, the built-in electric field can facilitate separation of charges (electrons and holes) in bulk, and promote their transfer to the catalyst surface, making them effective tools

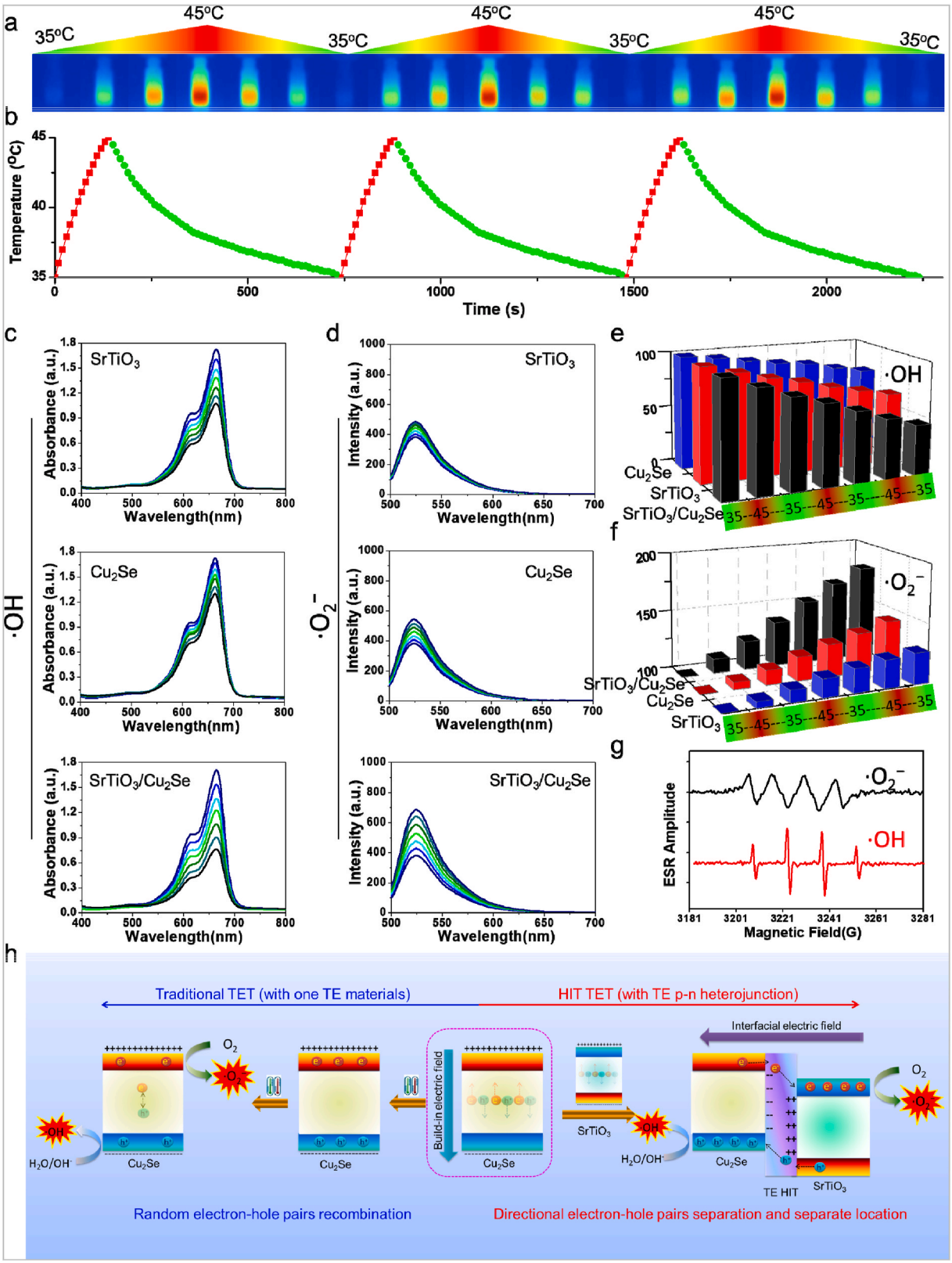

Fig. 3. ROS generation and mechanism of TET. (a) Photothermal images of $SrTiO_3/Cu_2Se$ NSs under 808 nm laser irradiation. (b) photothermal conversion of $SrTiO_3/Cu_2Se$ NSs under 808 nm laser irradiation. (c) and (e) $\cdot O_2^-$ generation of $SrTiO_3/Cu_2Se$ NSs under temperature gradient from 35 °C to 45 °C. (d) and (f) ·OH generation of $SrTiO_3/Cu_2Se$ NSs under temperature gradient from 35 °C to 45 °C. (g) The signal of ROS generated by $SrTiO_3/Cu_2Se$ NPs in EPR spectra. (h) The mechanism of $SrTiO_3/Cu_2Se$ NSs mediated TET.

for catalyzing reduction and oxidization of O_2 and H_2O to generate superoxide anion ($\cdot O_2^-$) and hydroxyl radical (·OH), respectively. $\cdot O_2^-$ generation through the reduction of electrons was measured with dihydrorhodamine 123 (DHR 123) probe. As shown in Fig. 3c and e, obvious fluorescence increase was detected following the temperature gradient (35 °C–45 °C) using $SrTiO_3$ NPs and Cu_2Se QDs separately, which indicated that $SrTiO_3$ NPs and Cu_2Se QDs are suitable nanomedicines for thermoelectric therapy. Of note, a much stronger fluorescence increase was observed when $SrTiO_3/Cu_2Se$ NPs were applied as thermoelectric catalysts for catalyzing $\cdot O_2^-$ generation from O_2. As exhibited in Fig. 3h, after $SrTiO_3$ NPs (n type) contacting with Cu_2Se QDs (p type), an interfacial electric field was then constructed on their interface, in which the separated electrons and holes induced by thermoelectric effect further transferred and re-located on the surface of different catalysts following interfacial electric field. Thereby, the recombination of electrons and holes was restricted, leading to extending lifetime of separated electrons and holes for further redox reactions. The p-n heterojunction enhanced thermoelectric effect of $SrTiO_3/Cu_2Se$ NPs was further assessed in terms of hydroxyl radical (·OH) production using methylene blue (MB) as the specific probe of ·OH. Consistent with the above results, the $SrTiO_3/Cu_2Se$ NPs exhibited the strongest ·OH generation, which further confirmed their p-n heterojunction enhanced thermoelectric effects (Fig. 3d and f). By employing 5,5-dimethyl-1-pyrroline N-oxide as the spin trapping agent, electron spin resonance (ESR) was applied to detect the generated ROS directly. As shown in Fig. 3g, $\cdot O_2^-$ and ·OH synchronously generated from $SrTiO_3/Cu_2Se$ NPs through thermoelectric effects from O_2 and H_2O were detected, which further confirms the high ability of ROS generation of $SrTiO_3/Cu_2Se$ NPs. In order to detect the potential application of $SrTiO_3/Cu_2Se$ NPs in clinic, the light-thermal-electricity-chemical energy conversion of $SrTiO_3$ NPs, Cu_2Se QDs, and $SrTiO_3/Cu_2Se$ NPs were also tested under irradiation of 808 nm laser at 0.33 W/cm^2. As shown in Fig. S7, the ROS generation performance, including $\cdot O_2^-$ and ·OH, were similar with that under irradiation of 808 nm laser at 1 W/cm^2, which showed a huge potential for clinical application. In addition, in order to confirm the ROS generation was resulted from the thermoelectric effect, the ROS generation performances were further detected through directly heating the $SrTiO_3$ NPs, Cu_2Se QDs, and $SrTiO_3/Cu_2Se$ NPs. As exhibited in Fig. S8, obvious ROS generations were observed and the yields of ROS were similar with that under irradiation of 808 nm laser at 1 or 0.33 W/cm^2, demonstrating the mechanism of ROS generation was the thermoelectric effect of thermoelectric materials.

3.3. In vitro antitumor evaluation mediated by $SrTiO_3/Cu_2Se$ NPs

The biocompatibility of the prepared TE agents was next tested using MCF 7 and Hela cancerous cells. As shown in Fig. 4a and S7, similar with the traditional photothermal agent (graphene, G), the TE agents showed negligible cytotoxicity in the absence of excitation, and more than 80% of the cells were viable even when exposed to 100 μg/mL of the respective TE agents. Stimulation with 808 nm laser led to the temperature increasing from 35 °C to 45 °C, and thus increased the cytotoxic effects of all TE agents (Fig. 4b and S8). However, under the uniform 808 nm laser irradiation and temperature increase, the cells treated with G still remain a relatively high viability. To this end, we speculated that the cytotoxic effects of TE agents are probably attributed to the thermoelectric effect inducing ROS generation, rather than photothermal effect inducing thermal. With increasing cycles of this temperature gradient (35 °C–45 °C), an enhanced cell cytotoxic effects of TE agents were observed, meanwhile, the cytotoxic effects of G remain negligible improved. This observation further demonstrated the thermoelectric effect of TE agents inducing ROS generation was the main cause for their cytotoxicity. Moreover, the cells treated with $SrTiO_3/Cu_2Se$ NPs exhibited the highest cytotoxicity, confirming the p-n heterojunction enhanced thermoelectric effect. Additionally, the intracellular ROS levels under different treatments were analyzed by using fluorescent probe. Indeedly, the intracellular ROS levels were significantly higher in the $SrTiO_3$ NPs and Cu_2Se QDs treated groups, compared to those treated with G, and the highest ROS concentration was detected in cells exposed to the $SrTiO_3/Cu_2Se$ NPs coupled with 808 nm laser irradiation and a natural cooling process (Fig. 4d and e). As previously reported [44], DNA damage caused by ROS is one of the main causes for ROS-induced cell toxicity. Thus, the levels of DNA damage in MCF 7 cells after different treatments were further analyzed using γ-H2AX as a marker for DNA double-strand breaks. As shown in Fig. 4f, MCF 7 cells treated with G with ΔT (35 °C–45 °C) did not show any obvious DNA damage compared with the control group. However, MCF 7 cells treated with $SrTiO_3$ NPs or Cu_2Se QDs coupling with the same ΔT, showed apparently detectable levels of DNA damage, further supporting the TE effect of $SrTiO_3$ NPs and Cu_2Se QDs. Treatment with $SrTiO_3/Cu_2Se$ NPs and ΔT produced considerably high levels of irreparable DNA damage in the cancer cells. All these results thus suggest that the developed therapeutic strategy based on $SrTiO_3/Cu_2Se$ NPs and ΔT with an enhanced TE effect can specifically kill cancer cells. Moreover, the efficient apoptosis of $SrTiO_3/Cu_2Se$ NPs *via* TE effect was further detected through co-staining cells with propidium iodide (PI, dead cells, red fluorescence) and calcein AM (live cells, green fluorescence) after different treatments. The LSCM images of co-stained cancer cells, as shown in Fig. 4g, also confirmed the antitumor effect of TET *in vitro*.

3.4. In vivo antitumor evaluation mediated by $SrTiO_3/Cu_2Se$ NPs

The anti-cancer potential of TET was next evaluated *in vivo* using MCF 7 tumor-bearing mice. The mice were each injected intravenously with Cy7-labeled NPs at the dosage of 5 mg/kg, and the fluorescence intensity of Cy7 in the blood was measured at different time intervals. As shown in Fig. 5b, the Cy7-loaded NPs remained significantly longer in circulation compared to free Cy7, which was suggestive of greater tumor accumulation of NPs. Additionally, the tumor accumulation of NPs was also confirmed by fluorescence imaging of major organs after 24 h *i.v.* injection (Fig. 5c). To more precisely characterize the biodistribution of NPs *in vivo*, an ICP was employed to test the concentration of NPs in the major organs and tumors over 24 h, which also showed a great tumor accumulation of the prepared NPs. The MCF 7 tumor-bearing mice were randomly divided into the following groups and treated accordingly: 1) saline control, 2) $SrTiO_3/Cu_2Se$ NPs, 3) $SrTiO_3$ NPs + ΔT, 4) Cu_2Se QDs + ΔT, 5) $SrTiO_3/Cu_2Se$ NPs + ΔT, 6) G + ΔT, and 7) PTT (G, >55 °C). The ΔT means temperature gradient (35 °C–45 °C) for 3 cycles inducing by 808 nm laser irradiation and natural cooling after 24 h post injection (Fig. 5a and e). The tumor volume was measured every 2 days, and as shown in the growth curves in Fig. 5f and g, the untreated and non-ΔT controls did not show any significant inhibition of tumor growth. The combination of TE agents ($SrTiO_3$ NPs or Cu_2Se QDs) and ΔT achieved an obvious inhibitory effect, which is attributed to the generation of ROS by the thermoelectric effect. Due to the p-n heterojunction enhanced thermoelectric effect, $SrTiO_3/Cu_2Se$ NPs with ΔT markedly inhibited tumor growth, in which $SrTiO_3/Cu_2Se$ NPs almost completely ablated the tumors under the same conditions. In contrast, the G NSs with the same ΔT treatment exhibited only a slight inhibition of tumor growth compared with the control group, which indicated the temperature of 45 °C can not able to induce cancer cells death. Only the hyperthermia (>55 °C) induced by G NSs-mediated PTT could provide a similar antitumor effect as that of TET (45 °C) (Fig. 5h). However, as shown in Fig. 5g, because the hyperthermia (>55 °C) randomly propagated and diffused to the surrounding tissues, an obvious PTT-related toxicity and side effects on normal tissues was observed, in which the skin and muscle at the 808 nm laser irradiation site were scorched. By contrast, there was negligible damage to the skin at the irradiated sites of TET (45 °C) (Fig. 5f). These findings are consistent with the thermoelectric effect and heterojunction structure of $SrTiO_3/Cu_2Se$ NPs that induces an intracellular ROS burst. The representative images of mice from the different treatments are shown in Fig. 5f and g. Moreover, the mice

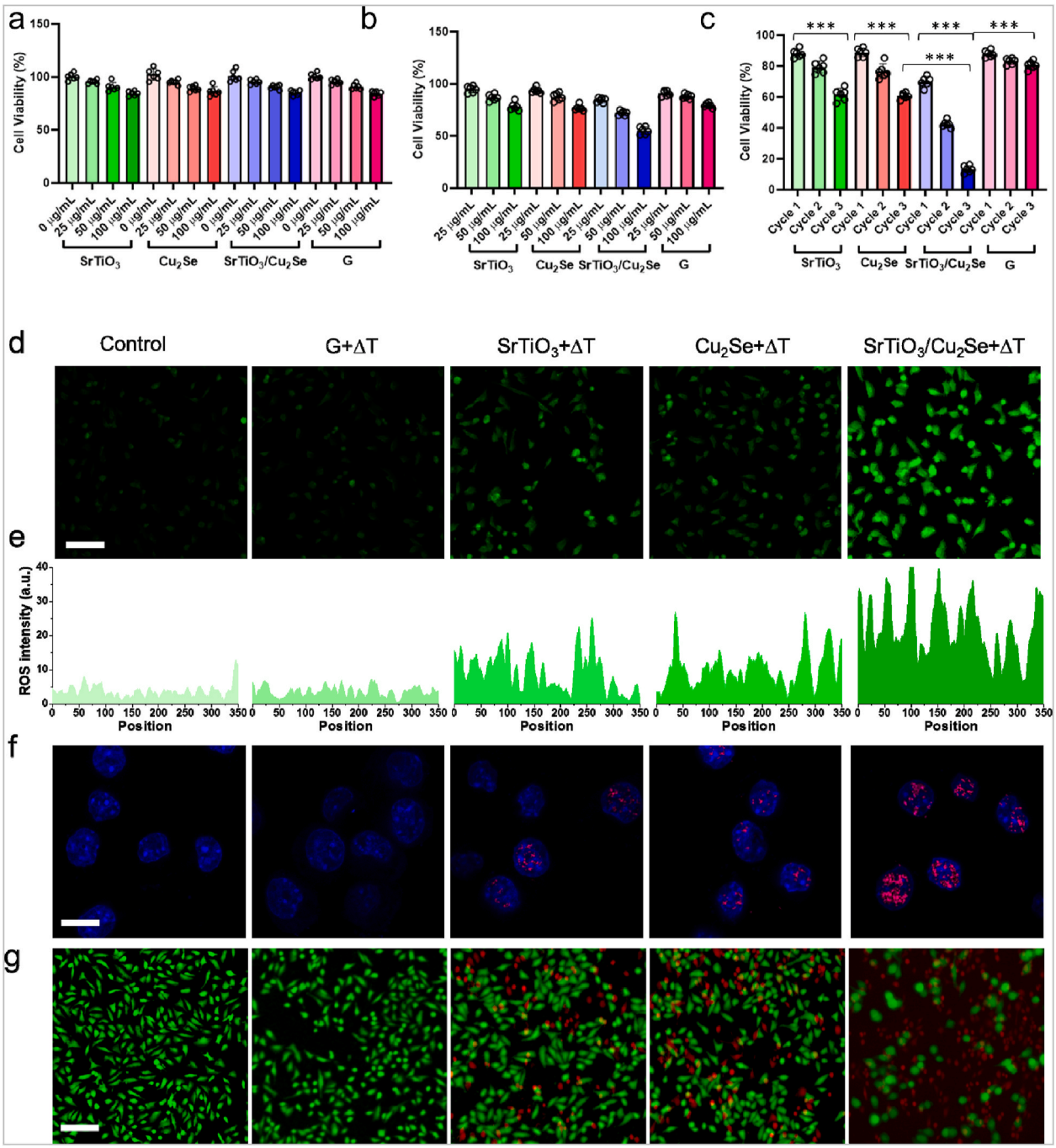

Fig. 4. ***In vitro*** **TET.** (a) Human breast cancer cells (MCF 7) viability treated with $SrTiO_3$ NSs, Cu_2Se NPs, and $SrTiO_3/Cu_2Se$ NSs at different concentrations for 24 h. The data show mean ± s.d., $n = 6$ biologically independent cells. (b) human breast cancer cells (MCF 7) viability treated with $SrTiO_3$ NSs, Cu_2Se NPs, and $SrTiO_3/Cu_2Se$ NSs and 808 nm laser at different concentrations for 24 h. The data show mean ± s.d., $n = 6$ biologically independent cells. (c) Antitumor effect of $SrTiO_3$ NSs, Cu_2Se NPs, and $SrTiO_3/Cu_2Se$ NSs based TET under different temperature gradient cycles. The data show mean ± s.d., $n = 6$ biologically independent cells. (d) CLSM images of ROS content in MCF 7 cells under different treatments. Scale bar = 100 μm. (e) Fluorescence quantitative analysis of the intracellular ROS in Fig. d. (f) Representative CLSM images of the MCF 7 cells after different treatments. Scale bar = 20 μm. The nuclei were stained by DAPI (blue), and the γH2AX foci per nucleus were stained by anti-γH2AX antibody (red). (g) Live/Dead cell staining assay in MCF 7 cells after different treatments (green, live cells; red, dead cells). Scale bar = 100 μm.

treated with $SrTiO_3/Cu_2Se$ NPs + ΔT showed the longest lifetime without any tumor recurrence (Fig. 5l). No significant changes were observed in the body weight of the mice during the experimental period (Fig. S10), indicating negligible adverse effects of this therapy *in vivo*.

The intracellular ROS burst effect was further validated by using DCFH fluorescence probe. As shown in Fig. 5i and S11, the different treatments led to consistent ROS accumulation in the tumors, and the strongest green fluorescence was detected in the $SrTiO_3/Cu_2Se$ NPs + ΔT group, further indicating a drastic ROS burst in tumor cells. Given that ROS induce apoptosis through DNA damage [44], we next analyzed the tumors for signs of DNA double strand breaks, oxidative stress and apoptosis. $SrTiO_3/Cu_2Se$ NPs alone induced negligible γ-H2AX foci and very few apoptotic cells, whereas both DNA damage and apoptosis were considerably higher under $SrTiO_3$ NPs or Cu_2Se QDs with ΔT. Coupling

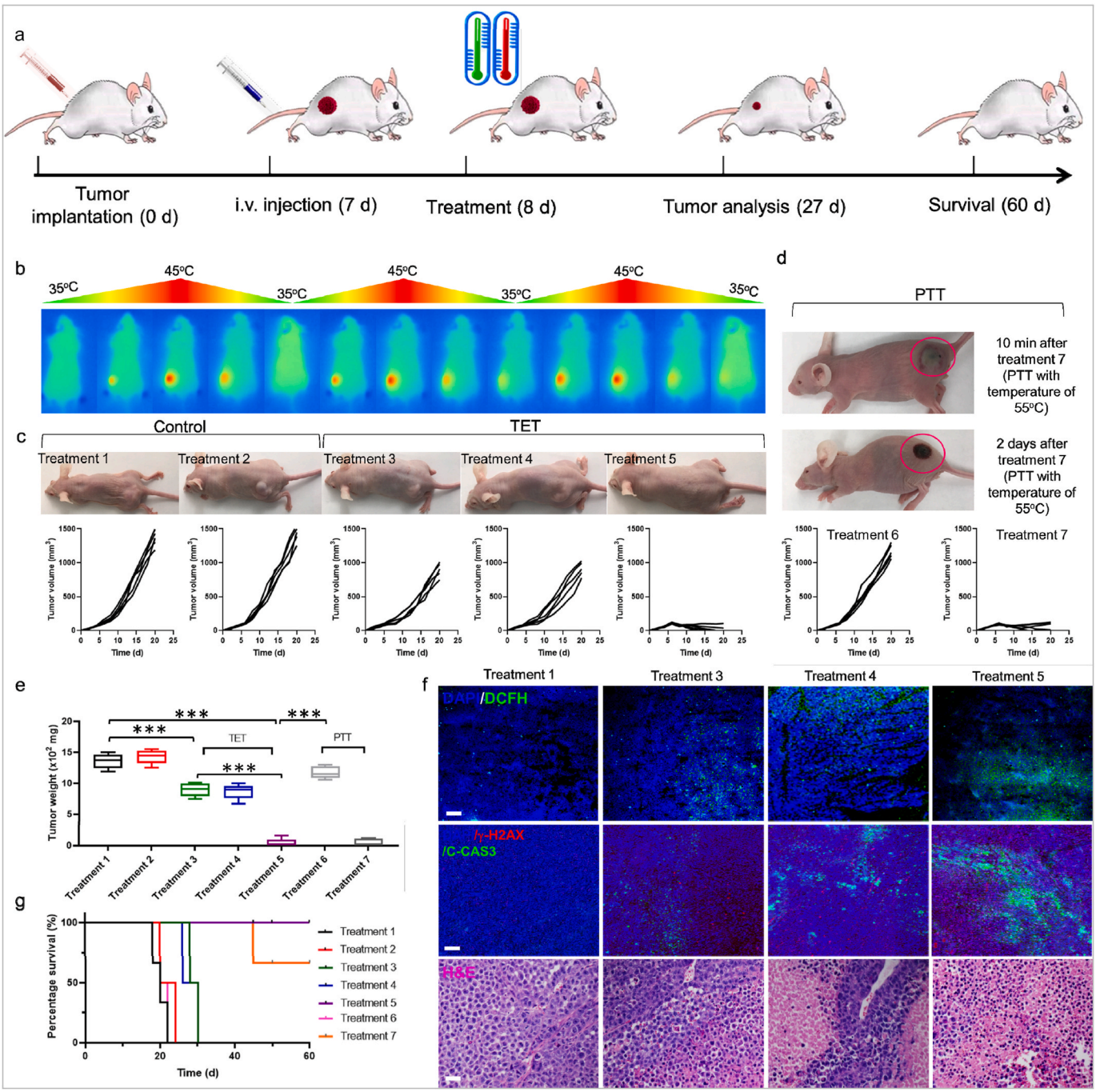

Fig. 5. ***In vivo*** **imaging, biodistribution, and anti-tumor study.** (a) Schematic illustration of treatment schedule. (b) Blood circulation performance of NPs-Cy7 and free Cy7. The data show mean ± s.d., $n = 3$ biologically independent animals. (c) Fluorescence images of major organs with i.v. injection of Cy 7 functionalized $SrTiO_3/Cu_2Se$ NPs. (d) Biodistribution of $SrTiO_3/Cu_2Se$ NPs in MCF 7 tumor-bearing mice by ICP measurement. The data show mean ± s.d., $n = 3$ biologically independent mice. (e) Photothermal heating and natural cooling images of tumor-bearing nude mice. (f) Anti-tumor effects of TET. Treatment 1: PBS, Treatment 2: $SrTiO_3/Cu_2Se$ NPs, Treatment 3: $SrTiO_3$ NSs + ΔT, Treatment 4: Cu_2Se NPs + ΔT, and Treatment 5: $SrTiO_3/Cu_2Se$ NPs + ΔT. The injected doses of $SrTiO_3/Cu_2Se$ NPs, $SrTiO_3$ NPs, and Cu_2Se QDs were 6 mg/kg. (g) Traditional graphene mediated PTT. Treatment 6: graphene with temperature increase to 45 °C and Treatment 7: graphene with temperature increase to 55 °C. (h) Tumors weight after different treatments. The data show mean ± s.d., $n = 5$ biologically independent mice. (i) *In vivo* ROS detection in the sections from tumors by dihydroethidium (DHE) *via* fluorescence microscopy. (j) Immunofluorescence (IF) and (k) H&E staining in the sections from the tumors after different treatments. The nucleus was stained by DAPI (blue), damaged DNA was stained by γH2AX foci (red), and apoptotic cells were stained by apoptosis marker C-CAS3 (green). Scar bar = 100 μm. Three times each experiment was repeated independently with similar results. (l) The survival curves of MCF 7 tumor-bearing mice after different treatments.

$SrTiO_3/Cu_2Se$ NPs and ΔT led to a marked increase in γ-H2AX foci and apoptosis in the tumors (Fig. 5j and k). Furthermore, the levels of 8-hydroxy-2′-deoxyguanosine (8-OHdG), a marker of oxidized DNA, were consistent with that of γ-H2AX (Fig. S12). Taken together, the p-n TE agents heterojunction can efficiently trigger a ROS burst in cancer cells and induce apoptosis under a mild condition.

3.5. *Biocompatibility evaluation of $SrTiO_3/Cu_2Se$ NPs*

In order to more precisely characterize the metabolism of $SrTiO_3/$

Cu_2Se NPs *in vivo*, an inductively coupled plasma emission spectrometer (ICP) was employed to analyze the concentration of $SrTiO_3/Cu_2Se$ NPs in major organs and tumors over 30 days. Besides the accumulations in tumors, high accumulations of $SrTiO_3/Cu_2Se$ NPs were also found in other normal organs such as liver, lung, and kidneys. However, the accumulate $SrTiO_3/Cu_2Se$ NPs in normal organs could be gradually excreted by the body over time (Fig. S16). Moreover, the biocompatibility of TET was evaluated *via* hematological, histological and immunological indices. As shown in Fig. 6a–c, no obvious difference in ROS levels, DNA damage, apoptosis, and tissue damage were observed in normal tissues after treatment with $SrTiO_3/Cu_2Se$ NPs + ΔT compared with those treated with PBS, indicating a favorable biocompatibility of the $SrTiO_3/Cu_2Se$ NPs and TET in normal tissues. Moreover, the serum levels of IFN-γ, IL-6, TNF-α and IL-12+P40 were similar in the control and treated mice 12 and 24h post *i.v.* injection of $SrTiO_3/Cu_2Se$ NPs (10 mg/kg) (Fig. 6d). In addition, routine blood examination on days 1, 7 and 14 post-injection did not show any significant differences in aspartate aminotransferase (AST), alanine aminotransferase (ALT), white blood cells (WBC), blood urea nitrogen (BUN), alkaline phosphatase (ALP), red blood cells (RBC), platelet (PLT), Hemoglobin (HGB), mean corpuscular volume (MCV), creatinine (Cr), lymphocyte (LYM), hematocrit (HCT), and neutrophil (NEU) between the control and treated groups (Fig. 6e). Taken together, $SrTiO_3/Cu_2Se$ NPs and TET are biocompatible *in vivo*.

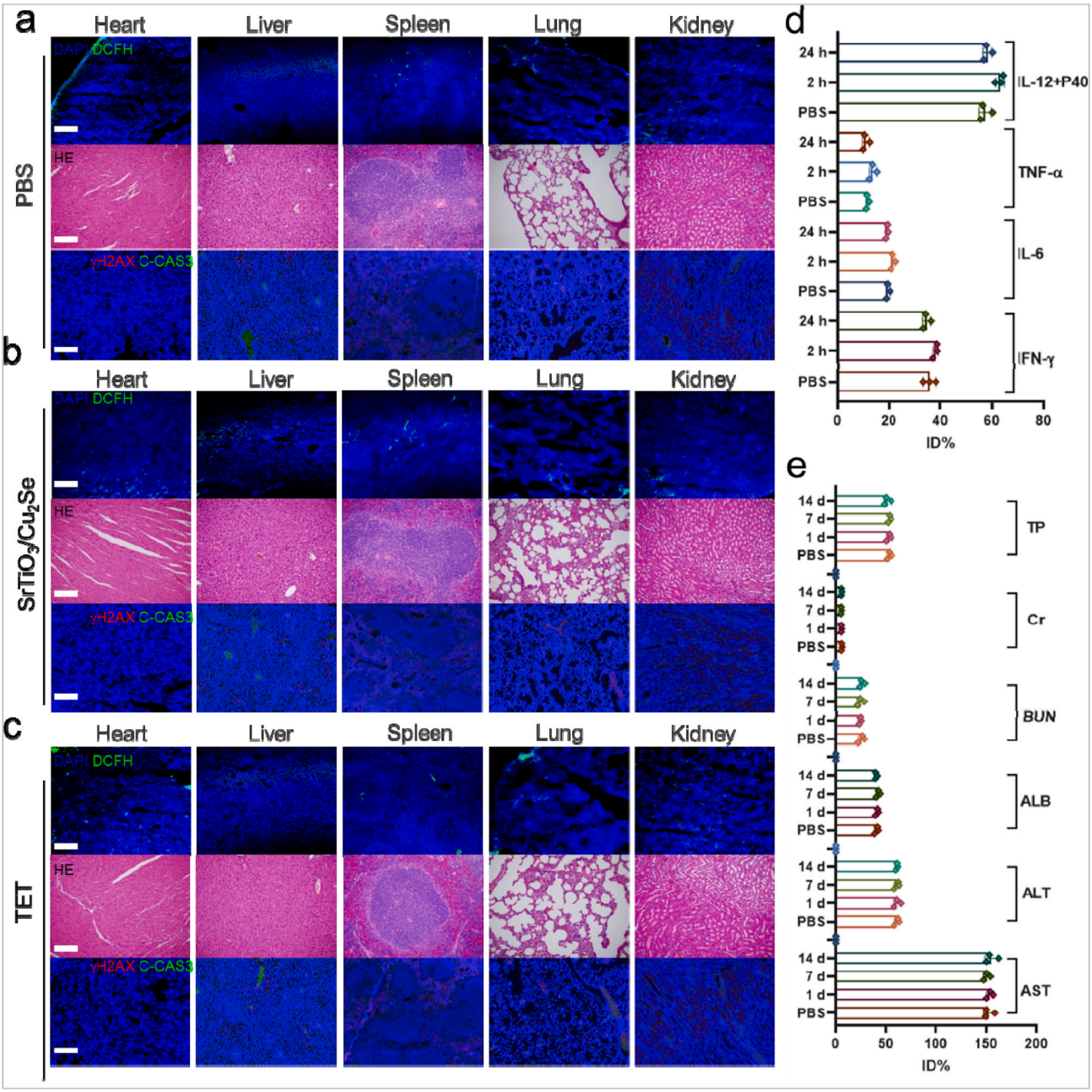

Fig. 6. *In vivo* toxicity of $SrTiO_3/Cu_2Se$ NPs and $SrTiO_3/Cu_2Se$ NPs mediated TET. H&E staining and immunofluorescence (IF) staining in the sections from the major organs, which were collected from the MCF 7 xenograft-tumor bearing mice after different treatments with (a) PBS, (b) $SrTiO_3/Cu_2Se$ NPs, and (c) $SrTiO_3/Cu_2Se$ NPs mediated TET. The nucleus was stained by DAPI (blue), damaged DNA was stained by γH2AX foci (red), and apoptotic cells were stained by apoptosis marker C-CAS3 (green). Scar bar = 100 μm. Three times each experiment was repeated independently with similar results. (d) Serum levels IFN-γ, IL-6, TNF-α, and IL-12+P40 in healthy mice at 2 or 24 h post intravenous injection of PBS or $SrTiO_3/Cu_2Se$ NPs. **e** Blood biochemistry and hematology analysis of Balb/c mice treated with PBS or $SrTiO_3/Cu_2Se$ NPs.

3.6. Comparation of side effects between PTT and TET

As demonstrated above, PTT with hyperthermia (>55 °C) could easily damage the skin at irradiated site. To further confirm the superiority of TET, we finally compared the treatment-related toxicity and side effects on normal tissues and organs through simulating the PTT and TET at some major organs and tissues. The PTT (55 °C) and TET (45 °C) related toxicity to major organs and tissues were simulated by directly exposing these organs and tissues to 55 °C and 45 °C. As exhibited in Fig. 7, exposure to the TET (45 °C) conditions, negligible toxicity or side effect are observed in their H&E staining images of heart, liver, spleen, lung, kidney, muscle, and skin, compared with these without any treatment. However, obvious and serious damages were revealed in these important organs and tissues after exposing to the PTT (55 °C) conditions. For example, congestion, enlargement of intercellular space, tissue defect, etc., were presented in these major organs. Additionally, evident swelling and critical damage were also observed in muscle and skin under treated with PTT (55 °C). All above phenomena further confirmed the *in vivo* safety of TET and demonstrated competitive advantages over PTT.

4. Conclusions

Cancer therapies based on energy conversion, such as photothermal therapy (PTT, light-to-thermal energy conversion) and photodynamic therapy (PDT, light-to-chemical energy conversion) have attracted extensive attention in preclinical research. However, the PTT-related hyperthermia (>55 °C) damage to surrounding tissues and shallow penetration of PDT-applied light (visible region) prevent further advanced clinical practices. The thermoelectric therapy (TET) based on NIR-to- tepidity-chemical energy (ROS) conversion, not only effectively avoids the defects of PTT and PDT, but also integrates the advantages of PTT and PDT. Here, a novel TET based on p-n heterojunction TE generator was successfully developed and demonstrated outstanding anticancer potency with negligible side-effects. The $SrTiO_3/Cu_2Se$ NPs based p-n heterojunction was prepared by simple two-step hydrothermal processes, exhibiting an excellent thermoelectric effect under mild temperature gradient from 35 °C to 45 °C. The formation of build-in electric field induced by thermoelectric effect under temperature gradient allowed directional separation of electrons and holes in the bulk of $SrTiO_3$ NPs and Cu_2Se QDs. Furthermore, the interfacial electric field induced by contacting of $SrTiO_3$ NPs (n type) and Cu_2Se QDs (p type) further guided the distribution and re-location of the excited electrons and holes onto the surface of $SrTiO_3$ NPs and Cu_2Se QDs, respectively. The synergy between build-in and interfacial electric fields facilitated the electrons and holes separation and transfer both in the bulk and the interface, minimizing the undesired charge recombination. Under 808 nm laser irradiation and natural cooling induced temperature

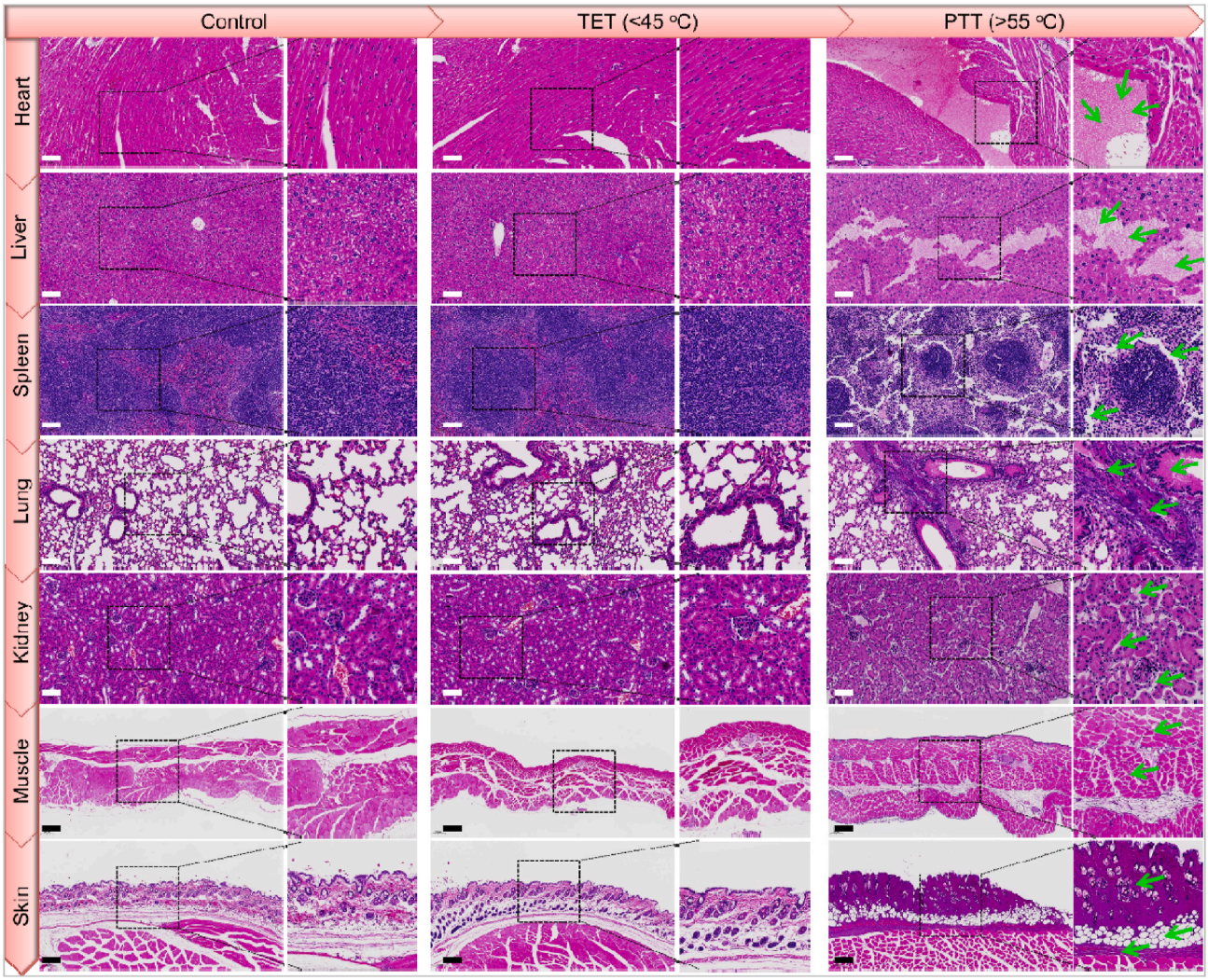

Fig. 7. H&E staining of major organs and tissues contacted with different temperature stimulating the potential damages of TET and traditional PTT to nearby organs and tissues. Scar bars = 500 μm.

gradient (35–45 °C), the engineered $SrTiO_3/Cu_2Se$ NPs serve as an intelligent TE generator with dually independent ROS ($\cdot O_2^-$ and ·OH) generation through catalyzing the oxidation and reduction of O_2 and H_2O in tumor microenvironment. With an effective ROS burst mediated apoptosis of cancer cells both *in vitro* and *in vivo*, the p-n heterojunction TE generator based TET has been demonstrated to be a novel and potential clinic cancer treatment. This work is also expected to provide a smart strategy for the design of other p-n heterojunction TE generator with efficient charges separation and will inspire future studies in expanding their in-depth application, especially in other biomedical applications, such as diabetic ulcer treatment and wound infection resistance under temperature difference between the body and outside environment. In addition, with the vigorous development of tumor immunotherapy [45–48], the combination of thermoelectric therapy and immunotherapy can more effectively eliminate tumor in situ and effectively inhibit tumor recurrence and metastasis.

CRediT authorship contribution statement

Yong Kang: Methodology, Formal analysis, Writing – original draft. **Na Kong:** Software, Investigation, Writing – original draft. **Meitong Ou:** Validation. **Ying Wang:** Formal analysis. **Qicai Xiao:** Writing – review & editing. **Lin Mei:** Resources. **Bing Liu:** Resources. **Liqun Chen:** Conceptualization, Supervision. **Xiaobin Zeng:** Conceptualization, Writing – review & editing, Supervision, Funding acquisition. **Xiaoyuan Ji:** Conceptualization, Writing – review & editing, Supervision, Project administration, Funding acquisition.

Declaration of competing interest

The authors declare no conflict of interest.

Acknowledgements

This study was supported by the National Natural Science Foundation of China (No. 32122044, 32071322, and 32000815); Science, Technology & Innovation Commission of Shenzhen Municipality (No. JCYJ20210324113004010 and RCBS20200714114855313). All animal experiments were performed according to protocols approved by the Institutional Animal Care and Use Committee of Sun Yat-sen University (Guangzhou, China).

Appendix A. Supplementary data

Supplementary data to this article can be found online at https://doi.org/10.1016/j.bioactmat.2022.07.007.

References

[1] J. Li, D. Cui, Y. Jiang, J. Huang, P. Cheng, K. Pu, Near-infrared photoactivatable semiconducting polymer nanoblockaders for metastasis-inhibited combination cancer therapy, Adv. Mater. 31 (2019), 1905091, https://doi.org/10.1002/adma.201905091.

[2] B. Ding, P. Zheng, P.a. Ma, J. Lin, Manganese oxide nanomaterials: synthesis, properties, and theranostic applications, Adv. Mater. 32 (2020), 1905823, https://doi.org/10.1002/adma.201905823.

[3] X. Cui, Z. Zhang, Y. Yang, S. Li, C.-S. Lee, Organic radical materials in biomedical applications: state of the art and perspectives. Explorations 2(2022), 20210264, 10.1002/EXP.20210264.

[4] X.Y. Wong, A. Sena-Torralba, R. Alvarez-Diduk, K. Muthoosamy, A. Merkoci, Nanomaterials for nanotheranostics: tuning their properties according to disease needs, ACS Nano 14 (2020) 2585–2627, https://doi.org/10.1021/acsnano.9b08133.

[5] S.S. Lucky, K.C. Soo, Y. Zhang, Nanoparticles in photodynamic therapy, Chem. Rev. 115 (2015) 1990–2042, https://doi.org/10.1021/cr5004198.

[6] X. Huang, W. Zhang, G. Guan, G. Song, R. Zou, J. Hu, Design and functionalization of the NIR-responsive photothermal semiconductor nanomaterials for cancer theranostics, Accounts Chem. Res. 50 (2017) 2529–2538, https://doi.org/10.1021/acs.accounts.7b00294.

[7] L. Zhao, Y. Liu, R. Xing, X. Yan, Supramolecular photothermal effects: a promising mechanism for efficient thermal conversion, Angew. Chem., Int. Ed. 59 (2020) 3793–3801, https://doi.org/10.1002/anie.201909825.

[8] X. Li, N. Kwon, T. Guo, Z. Liu, J. Yoon, Innovative strategies for hypoxic-tumor photodynamic therapy, Angew. Chem., Int. Ed. 57 (2018) 11522–11531, https://doi.org/10.1002/anie.201805138.

[9] P.-C. Lo, M. Salome Rodriguez-Morgade, R.K. Pandey, D.K.P. Ng, T. Torres, F. Dumoulin, The unique features and promises of phthalocyanines as advanced photosensitisers for photodynamic therapy of cancer, Chem. Soc. Rev. 49 (2020) 1041–1056, https://doi.org/10.1039/c9cs00129h.

[10] K. Wanderi, Z. Cui, Organic fluorescent nanoprobes with NIR-IIb characteristics for deep learning. Explorations 2(2022), 20210097, 10.1002/EXP.20210097.

[11] G. Liu, J. Zhu, H. Guo, A. Sun, P. Chen, L. Xi, W. Huang, X. Song, X. Dong, Mo2C-Derived polyoxometalate for NIR-II photoacoustic imaging-guided chemodynamic/photothermal synergistic therapy, Angew. Chem., Int. Ed. 58 (2019) 18641–18646, https://doi.org/10.1002/anie.201910815.

[12] H. Zhang, W. Zeng, C. Pan, L. Feng, M. Ou, X. Zeng, X. Liang, M. Wu, X. Ji, L. Mei, SnTe@MnO_2-SP nanosheet-based intelligent nanoplatform for second near-infrared light-mediated cancer theranostics, Adv. Funct. Mater. 29 (2019), 1903791, https://doi.org/10.1002/adfm.201903791.

[13] C. Xu, K. Pu, Second near-infrared photothermal materials for combinational nanotheranostics, Chem. Soc. Rev. 50 (2020) 1111, https://doi.org/10.1039/d0cs00664e.

[14] H. Zhou, X. Zeng, A. Li, W. Zhou, L. Tang, W. Hu, Q. Fan, X. Meng, H. Deng, L. Duan, Y. Li, Z. Deng, X. Hong, Y. Xiao, Upconversion NIR-II fluorophores for mitochondria-targeted cancer imaging and photothermal therapy, Nat. Commun. 11 (2020) 6183, https://doi.org/10.1038/s41467-020-19945-w, 6183.

[15] J. Li, R. Jiang, Q. Wang, X. Li, X. Hu, Y. Yuan, X. Lu, W. Wang, W. Huang, Q. Fan, Semiconducting polymer nanotheranostics for NIR-II/Photoacoustic imaging-guided photothermal initiated nitric oxide/photothermal therapy, Biomaterials 217 (2019), 119304, https://doi.org/10.1016/j.biomaterials.2019.119304.

[16] C. Yang, M.R. Younis, J. Zhang, J. Qu, J. Lin, P. Huang, Programmable NIR-II photothermal-enhanced starvation-primed chemodynamic therapy using glucose oxidase-functionalized ancient pigment nanosheets, Small 16 (2020), 2001518, https://doi.org/10.1002/smll.202001518.

[17] Q. Zhang, Q. Guo, Q. Chen, X. Zhao, S.J. Pennycook, H. Chen, Highly efficient 2D NIR-II photothermal agent with fenton catalytic activity for cancer synergistic photothermal-chemodynamic therapy, Adv. Sci. 7 (2020), 1902576, https://doi.org/10.1002/advs.201902576.

[18] W. Zhang, W. Deng, H. Zhang, X. Sun, T. Huang, W. Wang, P. Sun, Q. Fan, W. Huang, Bioorthogonal-targeted 1064 nm excitation theranostic nanoplatform for precise NIR-IIa fluorescence imaging guided efficient NIR-II photothermal therapy, Biomaterials 243 (2020), 119934, https://doi.org/10.1016/j.biomaterials.2020.119934.

[19] Q. Zhang, Y. Sun, W. Xu, D. Zhu, Organic thermoelectric materials: emerging green energy materials converting heat to electricity directly and efficiently, Adv. Mater. 26 (2014) 6829–6851, https://doi.org/10.1002/adma.201305371.

[20] A.D. Avery, B.H. Zhou, J. Lee, E.-S. Lee, E.M. Miller, R. Ihly, D. Wesenberg, K. S. Mistry, S.L. Guillot, B.L. Zink, Y.-H. Kim, J.L. Blackburn, A.J. Ferguson, Tailored semiconducting carbon nanotube networks with enhanced thermoelectric properties, Nat. Energy 1 (2016), 16033, https://doi.org/10.1038/nenergy.2016.33.

[21] J. Zhang, L. Song, G.K.H. Madsen, K.F.F. Fischer, W. Zhang, X. Shi, B.B. Iversen, Designing high-performance layered thermoelectric materials through orbital engineering, Nat. Commun. 7 (2016), 10892, https://doi.org/10.1038/ncomms10892.

[22] F. Kim, B. Kwon, Y. Eom, J.E. Lee, S. Park, S. Jo, S.H. Park, B.-S. Kim, H.J. Im, M. H. Lee, T.S. Min, K.T. Kim, H.G. Chae, W.P. King, J.S. Son, 3D printing of shape-conformable thermoelectric materials using all-inorganic Bi_2Te_3-based inks, Nat. Energy 3 (2018) 301–309, https://doi.org/10.1038/s41560-017-0071-2.

[23] Y. Ding, Y. Qiu, K. Cai, Q. Yao, S. Chen, L. Chen, J. He, High performance n-type Ag2Se film on nylon membrane for flexible thermoelectric power generator, Nat. Commun. 10 (2019) 841, https://doi.org/10.1038/s41467-019-08835-5.

[24] P. Qiu, T. Mao, Z. Huang, X. Xia, J. Liao, M.T. Agne, M. Gu, Q. Zhang, D. Ren, S. Bai, X. Shi, G.J. Snyder, L. Chen, High-efficiency and stable thermoelectric module based on liquid-like materials, Joule 3 (2019) 1538–1548, https://doi.org/10.1016/j.joule.2019.04.010.

[25] Y. Zhang, X. Gao, Y. Wu, J. Gui, S. Guo, H. Zheng, Z. L. Wang, Self-powered technology based on nanogenerators for biomedical applications. Explorations 1 (2021), 90-114, 10.1002/EXP.20210152.

[26] C. Pan, M. Ou, Q. Cheng, Y. Zhou, Y. Yu, Z. Li, F. Zhang, D. Xia, L. Mei, X. Ji, Z-scheme heterojunction functionalized pyrite nanosheets for modulating tumor microenvironment and strengthening photo/chemodynamic therapeutic effects, Adv. Funct. Mater. 30 (2020), 1906466, https://doi.org/10.1002/adfm.201906466.

[27] P. Zhu, Y. Chen, J. Shi, Piezocatalytic tumor therapy by ultrasound-triggered and $BaTiO_3$ -mediated piezoelectricity, Adv. Mater. 32 (2020), 2001976, https://doi.org/10.1002/adma.202001976.

[28] R. Chen, J. Lee, W. Lee, D. Li, Thermoelectrics of nanowires, Chem. Rev. 119 (2019) 9260–9302, https://doi.org/10.1021/acs.chemrev.8b00627.

[29] G. Tan, L.-D. Zhao, M.G. Kanatzidis, Rationally designing high-performance bulk thermoelectric materials, Chem. Rev. 116 (2016) 12123–12149, https://doi.org/10.1021/acs.chemrev.6b00255.

[30] X.-L. Shi, J. Zou, Z.-G. Chen, Advanced thermoelectric design: from materials and structures to devices, Chem. Rev. 120 (2020) 7399–7515, https://doi.org/10.1021/acs.chemrev.0c00026.

[31] X. Ji, J. Wang, Y. Kang, L. Mei, Z. Su, S. Wang, G. Ma, J. Shi, S. Zhang, Enhanced solar energy harvest and electron transfer through intra- and intermolecular dual channels in chlorosome-mimicking supramolecular self-assemblies, ACS Catal. 8 (2018) 10732–10745, https://doi.org/10.1021/acscatal.8b03105.
[32] X. Ji, Y. Kang, T. Fan, Q. Xiong, S. Zhang, W. Tao, H. Zhang, An antimonene/Cp*Rh(phen)Cl/black phosphorus hybrid nanosheet-based Z-scheme artificial photosynthesis for enhanced photo/bio-catalytic CO_2 reduction, J. Mater. Chem. 8 (2020) 323–333, https://doi.org/10.1039/c9ta11167k.
[33] Y. Kang, Z. Li, Y. Yang, Z. Su, X. Ji, S. Zhang, Antimonene nanosheets-based Z-scheme heterostructure with enhanced reactive oxygen species generation and photothermal conversion efficiency for photonic therapy of cancer, Adv. Health. Mater. 10 (2020), 2001835, https://doi.org/10.1002/adhm.202001835.
[34] M. Ou, C. Pan, Y. Yu, X. Wang, Y. Zhou, H. Zhang, Q. Cheng, M. Wu, X. Ji, L. Mei, Two-dimensional highly oxidized ilmenite nanosheets equipped with Z-scheme heterojunction for regulating tumor microenvironment and enhancing reactive oxygen species generation, Chem. Eng. J. 390 (2020), 124524, https://doi.org/10.1016/j.cej.2020.124524.
[35] N. Kong, H. Zhang, C. Feng, C. Liu, Y. Xiao, X. Zhang, L. Mei, J.S. Kim, W. Tao, X. Ji, Arsenene-mediated multiple independently targeted reactive oxygen species burst for cancer therapy, Nat. Commun. 12 (2021) 4777, https://doi.org/10.1038/s41467-021-24961-5.
[36] Y. Kang, L. Lei, C. Zhu, H. Zhang, L. Mei, X. Ji, Piezo-photocatalytic effect mediating reactive oxygen species burst for cancer catalytic therapy, Mater. Horiz. 8 (2021) 2273–2285, https://doi.org/10.1039/d1mh00492a.
[37] Y. Chen, Z. Gao, F. Zhang, Z. Wen, X. Sun, Recent progress in self-powered multifunctional e-skin for advanced applications. Explorations 2(2022), 20210112, 10.1002/EXP.20210112.
[38] Y. Deng, Z. Luo, N.J. Conrad, H. Liu, Y. Gong, S. Najmaei, P.M. Ajayan, J. Lou, X. Xu, P.D. Ye, Black phosphorus-monolayer MoS_2 van der Waals heterojunction p-n diode, ACS Nano 8 (2014) 8292–8299, https://doi.org/10.1021/nn5027388.
[39] C.-H. Lee, G.-H. Lee, A.M. van der Zande, W. Chen, Y. Li, M. Han, X. Cui, G. Arefe, C. Nuckolls, T.F. Heinz, J. Guo, J. Hone, P. Kim, Atomically thin p-n junctions with van der Waals heterointerfaces, Nat. Nanotechnol. 9 (2014) 676–681, https://doi.org/10.1038/nnano.2014.150.
[40] R. Frisenda, A.J. Molina-Mendoza, T. Mueller, A. Castellanos-Gomez, H.S.J. van der Zant, Atomically thin p-n junctions based on two-dimensional materials, Chem. Soc. Rev. 47 (2018) 3339–3358, https://doi.org/10.1039/c7cs00880e.
[41] F. Hu, Q. Cai, F. Liao, M. Shao, S.-T. Lee, Recent advancements in nanogenerators for energy harvesting, Small 11 (2015) 5611–5628, https://doi.org/10.1002/smll.201501011.
[42] L. Guo, Q. Lu, Potentials of piezoelectric and thermoelectric technologies for harvesting energy from pavements, Renew. Sustain. Energy Rev. 72 (2017) 761–773, https://doi.org/10.1016/j.rser.2017.01.090.
[43] Y. Bai, H. Jantunen, J. Juuti, Energy harvesting research: the road from single source to multisource, Adv. Mater. 30 (2018), 1707271, https://doi.org/10.1002/adma.201707271.
[44] Y. Kang, Z. Mao, Y. Wang, C. Pan, M. Ou, H. Zhang, W. Zeng, X. Ji, Design of a two-dimensional interplanar heterojunction for catalytic cancer therapy, Nat. Commun. 13 (2022) 2425, https://doi.org/10.1038/s41467-022-30166-1.
[45] T. Yu, W. Nie, Z. Hong, Y. He, J. Chen, X. Mi, S. Yang, X. Li, B. Wang, Y. Lin, Synergy of immunostimulatory genetherapy with immune checkpoint blockade motivates immune response to eliminate cancer, Adv. Funct. Mater. 31 (2021), 2100715, https://doi.org/10.1002/adfm.202100715.
[46] X. Liu, B. Wang, Y. Li, Y. Hu, X. Li, T. Yu, Y. Ju, T. Sun, X. Gao, Y. Wei, Powerful anticolon tumor effect of targeted gene immunotherapy using folate-modified nanoparticle delivery of ccl19 to activate the immune system, ACS Cent. Sci. 5 (2019) 277–289, https://doi.org/10.1021/acscentsci.8b00688.
[47] Y. Ding, Y. Wang, Q. Hu, Recent advances in overcoming barriers to cell-based delivery systems for cancer immunotherapy. Explorations 2(2022), 20210106, 10.1002/EXP.20210106.
[48] W. Nie, T. Yu, X. Liu, B. Wang, X. Gao, Non-viral vector mediated CKb11 with folic acid modification regulates macrophage polarization and DC maturation to elicit immune response against cancer, Bioact. Mater. 6 (2021) 3678, https://doi.org/10.1016/j.bioactmat.2021.03.031.